



Water Heating Rate as a Function of Magnetic Field and Electrical Induction Using Solar Energy

Sanaa T. Mousa Al-Musawi¹, Monaem Elmnifi², Osama D.H. Abdulrazig², Atheer Raheem Abdullah³,
Lina Jassim⁴, Hasan Shakir Majdi⁵, Laith Jaafer Habeeb^{6*}

¹ Department of Reconstruction and Projects, University of Baghdad, Baghdad 10001, Iraq

² Department of Mechanical Engineering Faculty of Engineering, Bright Star University, Brega 00218, Libya

³ Department of Air-Conditioning and Refrigeration Eng. Tech., Al-Rafidain University College, Baghdad 10001, Iraq

⁴ Mechanical Engineering Department, Mustansiriyah University, Baghdad 10001, Iraq

⁵ Department of Chemical Engineering and Petroleum Industries, Al-Mustaqbal University College, Babylon 51001, Iraq

⁶ Training and Workshop Center, University of Technology-Iraq, Baghdad 10001, Iraq

Corresponding Author Email: Laith.J.Habeeb@uotechnology.edu.iq

Copyright: ©2024 The authors. This article is published by IETA and is licensed under the CC BY 4.0 license (<http://creativecommons.org/licenses/by/4.0/>).

<https://doi.org/10.18280/mmep.110204>

ABSTRACT

Received: 16 September 2023

Revised: 22 November 2023

Accepted: 3 December 2023

Available online: 27 February 2024

Keywords:

magnetic fields, water heating, solar electric induction, CFD

The effect of magnetic fields on the water remains a highly controversial topic despite much research focused on this topic in the past decades. However, the improvement of water heating in a magnetic field is less controversial. The mechanism underlying this phenomenon was studied in prior works. In this paper, use solar electric induction to study the heating of water in magnetic fields; one distinction between induction heating and magnetic field heating is that the convection in the water heater is varied due to the different heating locations. Using computational fluid dynamics, it was possible to examine the heat load in the heater during induction heating and magnetic field heating, determine its temperature distribution, and flow rate. The heat flow in magnetic field heating was measured over the heater base at the bottom. In induction heating, the analysis was conducted using the distribution of heat production as determined by electromagnetic field analysis. Simulation shows differences in convective flow in the heater during induction heating and magnetic field heating, particularly in the early stages of heating.

1. INTRODUCTION

According to various studies, a magnetic field (MF) can change the physical and chemical characteristics of water over a long period of time [1-9]. Water turns into magnetic water when it flows through MF (MW). They investigated the optical characteristics of water in the presence of two powerful magnets and discovered that the MW's infrared absorption property changed [2]. A study revealed that MF could improve conduction and lessen water's surface tension [3, 4]. Friction experiments were used to study how static MF affected liquid water, and the results showed that the coefficient of friction was lower in MF [5]. Examined how MF affected water's hydrogen bonding and analyzed the magnetization mechanism using molecular dynamics simulations, experimental data, and theoretical models [6-8]. Revealed how MF can speed up the breakdown of organic material in wastewater and paper pulp. When MFS varied from 0 MT to 900 MT, wastewater PH values first rose to a peak and then fell [9]. There is ongoing debate regarding how MF affects water quality, and it is unclear how MF is treated [1, 4, 6]. However, because to changes in physical and chemical qualities, MW has primarily been used in agriculture, industry, and building. It can, for instance, clean wastewater, encourage plant growth, stop

metal surfaces from rusting, and enhance concrete performance [9-12]. Despite the fact that several of the MF-impacted water qualities have the parameters of specific heat, quantity of evaporation, and megawatt boiling point, which are particularly essential in a variety of applications, including condensed systems, thermal power, and other sectors, are the focus of very few studies that have been recorded.

The use of electromagnetic induction heaters (IH) as an alternative to conventional heating has grown recently. IH only heats the top of the heater since electromagnetic induction is used to create heat in that area of the coil. The hot location in MF is different from that in IH because the bottom portion is heated. In that case, the location of the heating may have an impact on the heater's heat load. Therefore, different temperature schedules are needed in commercial equipment like furnaces and water heaters. CFD is a numerical method that has been used to handle the simultaneous transfer of heat, mass, and momentum (fluid flow) with boundary conditions imposed in a specific computational domain, from the standpoint of fluid engineering [12]. Many food processing procedures, such as chilling, drying, baking, mixing, freezing, heating, pasteurization, and sterilization, need the movement of liquids. Thanks to CFD techniques in the food business, food engineers now have new insights, awareness of the

potential performance of food equipment at the design stage, and confidence in the quality or safety of food items [13]. The application of CFD approaches to better understand the operation and design processes has led to improvements in a variety of equipment, including furnaces, heat exchangers, cryogenic display cabinets, and spray dryers [14]. These are only a few of the CFD's most significant applications in the food industry. Recent years have seen a lot of attention focused on natural convection in fluid-filled cylindrical, square bore, and rectangular containers. Natural convection was investigated in all of the aforementioned scenarios utilizing either numerical analysis using the company's commercial CFD software or, in certain cases, open-source alongside experimental flow visualization and temperature measuring techniques [14-16]. The following are some examples of how CFD may be used to model convective flow used CFD to investigate the behavior of convection, temperature change, and airflow change in liquid meals during equation sterilization. Kumar et al. [17] investigated the fluid's temperature distribution and flow velocity distribution when the 3D pouches were heated and sterilized. In a horizontal tray during sterilization with CFD in 2002, numerical models predicted the assignment of temperature and transient velocity. A tube-type heat exchanger was used in 2003 to analyze the change in flow rate and temperature history during the sterilization of liquid meals [18]. Gandhi et al. [16] used CFD models and particle image observation to study natural single-phase convection and phase (boiling) coupled with temperature stratification. In terms of IH modeling, they explored the IH procedure using a non-contact measuring method based on thermal imaging and showed that thermogram measurements are useful tools for monitoring workpiece temperature distributions during IH. He evaluated a nonlinear and transient problem involving thermomagnetic coupling to a moving coil, which is a moving heat source, using an effective finite element method. The velocity, the inductor's beginning position, and the ratio of the inner to outer radius were all examined by researchers to see how they affected the temperature distribution [17]. In another article studied by Ghani et al. [18], new methods for numerically planning and optimizing IH treatment operations were presented.

As a result, CFD has been the subject of numerous studies as a convective flow-modeling tool [19, 20]. The variations in the phenomena of convection in a water heater during the heating process under IH and MF have not, however, been explored. In our earlier work, we saw and measured the flow through a solar-powered heater during IH and calculated the rated efficiency and power factor using a theoretical computing and simulation approach using CFD software. The simulation was run using a frequency heating coil system and an induction heating system at temperatures between 11 and 55°C (50 Hz, 3 kW). The flow rates in the tubes were 0.113 kg/sec and 0.134 kg/sec in the vessels. Efficiency and power factor of the induction water heater were measured, and the results were confirmed to be accurate [21, 22].

Advantages Unlike traditional heating technology that requires physical contact, magnetic induction heating has a number of advantages: Precise heat regulation and diffusion in the object to be heated. Where heat is transmitted more quickly along the body compared to traditional convection, magnetized water is used in the manufacture of food packaging and prevents contamination in it, magnetized water increases the shelf life of food. Moreover, contributes to

increasing resources as it increases animal and plant growth, achieves a real safety fence for equipment, lines Production in food processing, and others against salts, corrosion factors, and rapid deterioration [23]. And its applications in steam production units, cooling, and heating, and the mechanics of this process is that when the water passes through an alternating magnetic field, it makes most of the materials suspended in the water, such as calcium, magnesium, and others, and prevents them from being deposited on the walls of the pipes, and the magnetic energy works to prevent oxygen from attacking the metal and preventing corrosion. It gives a high flow rate, effectively controls corrosion, breaks down acids, and does not require cleaning chemicals [24]. It is used in water treatment methods. It was found that a magnetic field of strength ranging from 100 to 1000 gauss is considered effective in reducing the formation of a scaling layer on boilers and heating systems after magnetic treatment. The magnetic field inhibits microorganisms that cause food spoilage. This method was used to treat milk, yogurt, orange juice, and dough. In milk, the total count of microbes decreased from 25000 to 970 colonies/mL at a field strength of 12 Tesla, and in yogurt, it decreased from 3500 to 25 colonies/mL when exposed to a field strength of 40 Tesla. In orange juice, the total count of microbes decreased from 25000 to 6 colonies/mL at a field strength of 40 Tesla, as well as in the dough decreased from 3000 to 1 colony/ml at a field strength of 7.5 Tesla. The chlorine odor is greatly reduced after the water is magnetically treated [25].

Due to the constant search for alternatives to traditional energy from fossil fuels and gas due to the resulting pollution and carbon emissions that increase global warming, comes thinking about renewable energy and the possibility of using it in various fields [26]. An alternative to electric current for domestic heating, with a motor to generate a magnetic field to provide a temperature deficit in the electric induction's inability to meet the heating rate. In this study, IH and MF used flow visualization and simulation using CFD to examine the phase heat transfer by natural convection inside a water heater in terms a temperature time and convective flow velocity. We used software to simulate convective water flow in the geyser via IH and MF. Calculations were made for the lower and upper halves of the heater in order to speed up the computing process. It is very important to measure heat flux when the heating state changes since heat flux varies with different heating conditions. On the other hand, when we can estimate heat formation in IH using electromagnetic field analysis, we do not need to observe heat flux (EFA). The IH water carrier is then heated by dispersing the heat along a 200 mm, 16 mm diameter coil. The vortex heat is dispersed in a vessel with a diameter of 120 mm and a length of 250 mm. We hypothesized that in the MF heat distribution, a 0.08 mm thin layer of heat generation in a stainless steel bottom plate, at the base of a 100 mm diameter vessel, in a DC rotary motor, produces magnetic vortices to produce heat at the base of the heater. The distribution of heat generated at the base of the heater reaches 120°C.

The temperature distribution of IH similarly reaches 40°C. In the MF, a donut-shaped heating pattern was used to raise the temperature of the heated area at the bottom of the heater, which sits directly above the stationary magnet. The area around the bottom corner of the heater in the MF was warmer than the surrounding air. Since the coil covers the majority of the sides of the heater, the side heater has a high temperature. Therefore, only the underside was heated on IH, while a large

between 11 and 55°C. Due to the various heating techniques, the circumstances cannot be equalized. However, a thermal standard needs to be established in order to compare various heating systems to one another. In this research. To heat the water carrier, a 16 mm diameter by 200 mm long coil type is used to distribute heat. Distribute the heat of the vortex on a bowl with a diameter at 120 mm and a length at 250 mm. The minimal eddy current, which was located at corner of the work piece, represents a heating defect at the end and edge of the induction. In MF heat distribution, a DC spinning motor creates magnetic vortices at the base of the heater to produce heat. The heater has a diameter of 100 mm. The system is supplied with electric current via a solar panel.

2.1 Heating and heat flow in the heater

IH and MF heaters heat differently. The heat flow in the instance of MF was measured at the heater's base. The location of the heater's heat flow is depicted in Figure 3. IH's frequency

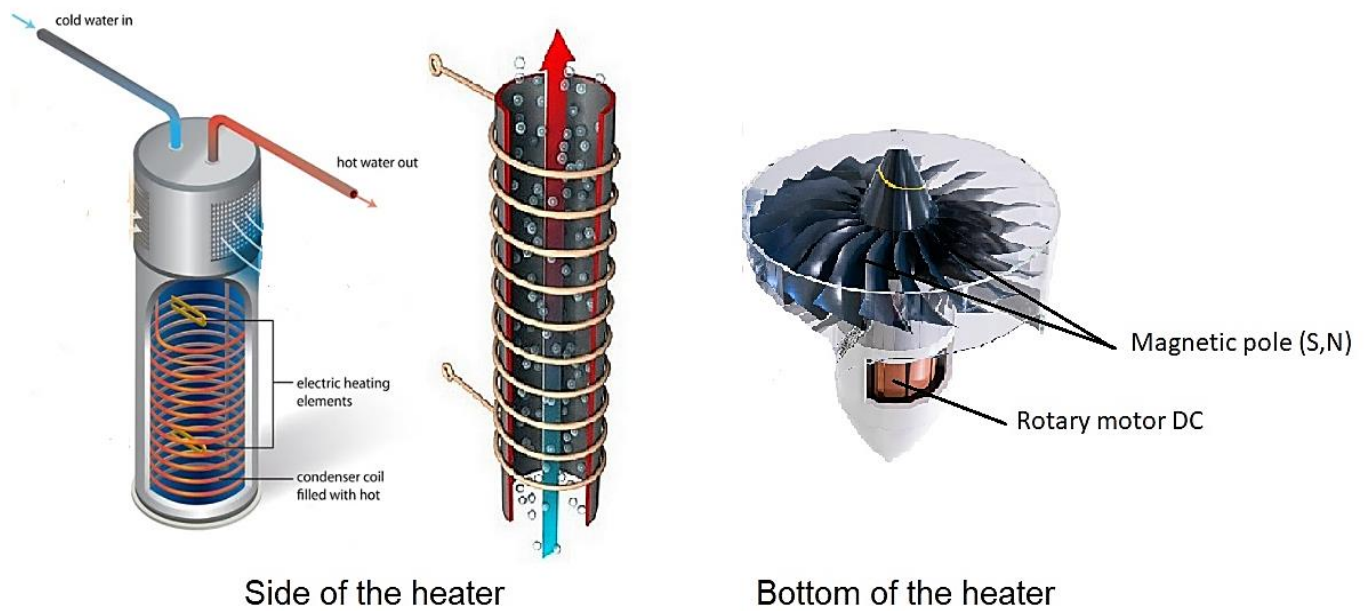


Figure 3. Design model of the heater side and bottom

The low temperatures in this study's early stage of water heating prevented the complicated behavior a water evaporation at the boiling point, therefore the presumption of in boiling (i.e., no phase change) was taken into consideration. We may reduce the complexity of the heating model by using the fact that when a liquid is below its boiling point, it evaporates off its surface and develops vapor bubbles that come from the liquid's bulk. These circumstances call for greater precision and care in the simulation of all factors related to boiling water.

2.1.1 Conditions and assumptions used in the simulation model

We presumed the heater had a cylinder-like shape in order to make the task simpler. Since the heating state is axially symmetric, the fluid convection in the heater may exhibit axial symmetry. assuming that the heater's interior wall is non-slip. Due to the fact that it was a natural transition brought on by heating, the convection in the heater was a laminar flow. The thermophysical characteristics of water were thought to be temperature dependent using the Rayleigh number (5.06×10^6

response was obtained in order to analyze the electromagnetic field. Using the electromagnetic properties of heater and vessel materials, such as heater cap, coil, and heater bottom materials, a 3D finite element model of the heat generation was created. Boiling causes a phase change in the water in the heater if the temperature is higher than the boiling point. The boiling point, however, cannot be determined using CFD. As a result, the CFD was assigned using the following temperature recovery procedure. For each point in the heater, a temperature variation with a boiling point was computed. If ΔT is greater than zero, latent heat is liberated from the sensible heat above the boiling point and is contributed to the equation of conservation of energy. This method can be used to calculate water temperatures up to 100°C. The air layer's temperature can also be determined, up to a maximum of 40°C. This 3D model was used for frequency response analysis to validate the typical values of heat generation. The CFD model is displayed in Figure 2.

- 9.4×10^6), and their values altered throughout CFD simulation. The Navier-Stokes equations are the partial differential equations that control the typical load and motion in a cylinder space. The cylinder's coordinates are displayed as follows [26]:

2.1.2 Basic equations

$$\frac{1}{r} \frac{\partial}{\partial r} (r \rho v_r) + \frac{1}{r} \frac{\partial}{\partial \theta} (\rho v_\theta) + \frac{\partial}{\partial z} (\rho v_z) = 0 \quad (1)$$

In order of simplify an analysis, the buoyant force due to the difference of density with temperature in the equations, the momentum equation in the radial direction (r), the continuity equation, the energy conservation equation [22].

$$\frac{\partial T}{\partial t} + v_r \frac{\partial T}{\partial r} + \frac{v_\theta}{r} \frac{\partial T}{\partial \theta} + v_z \frac{\partial T}{\partial z} = \frac{k}{\rho c_p} \left[\frac{1}{r} \frac{\partial}{\partial r} \left(r \frac{\partial T}{\partial r} \right) + \frac{1}{r^2} \frac{\partial^2 T}{\partial \theta^2} + \frac{\partial^2 T}{\partial z^2} \right] \quad (2)$$

$$\begin{aligned} & \rho \left(\frac{\partial v_r}{\partial t} + v_r \frac{\partial v_r}{\partial r} + \frac{v_\theta}{r} \frac{\partial v_r}{\partial \theta} - \frac{v_\theta^2}{r} + v_z \frac{\partial v_r}{\partial z} \right) \\ &= -\frac{\partial p}{\partial r} + \mu \left[\frac{\partial}{\partial r} \left(\frac{1}{r} \frac{\partial}{\partial r} (r v_r) \right) + \frac{1}{r^2} \frac{\partial^2 v_r}{\partial \theta^2} - \frac{2}{r^2} \frac{\partial v_\theta}{\partial \theta} + \frac{\partial^2 v_r}{\partial z^2} \right] \\ & \quad + \rho_{ref} g [1 - \beta(T - T_{ref})] \end{aligned} \quad (3)$$

The coefficient of thermal expansion of the liquid, the reference temperature and density, respectively T_{ref} , ρ_{ref} , in the direction of the axis (z). Also, the angular direction equation (θ) [26].

$$\begin{aligned} & \rho \left(\frac{\partial v_z}{\partial t} + v_r \frac{\partial v_z}{\partial r} + \frac{v_\theta}{r} \frac{\partial v_z}{\partial \theta} + v_z \frac{\partial v_z}{\partial z} \right) \\ &= -\frac{\partial p}{\partial z} + \mu \left[\frac{1}{r} \frac{\partial}{\partial r} \left(r \frac{\partial v_z}{\partial r} \right) + \frac{1}{r^2} \frac{\partial^2 v_z}{\partial \theta^2} + \frac{\partial^2 v_z}{\partial z^2} \right] \end{aligned} \quad (4)$$

$$\begin{aligned} & \rho \left(\frac{\partial v_\theta}{\partial t} + v_r \frac{\partial v_\theta}{\partial r} + \frac{v_\theta}{r} \frac{\partial v_\theta}{\partial \theta} + \frac{v_r v_\theta}{r} + v_z \frac{\partial v_\theta}{\partial z} \right) \\ &= -\frac{1}{r} \frac{\partial p}{\partial \theta} + \mu \left[\frac{\partial}{\partial r} \left(\frac{1}{r} \frac{\partial}{\partial r} (r v_\theta) \right) + \frac{1}{r^2} \frac{\partial^2 v_\theta}{\partial \theta^2} + \frac{2}{r^2} \frac{\partial v_r}{\partial \theta} + \frac{\partial^2 v_\theta}{\partial z^2} \right] \end{aligned} \quad (5)$$

In IH, the side wall of the heater is used as a heat transfer limit since heat is generated from its side wall. Following a CFD, we performed and assessed a heat transfer coefficient. A temperature of the water that had been heated in the heater was measured after it had been cooled solely along its side wall. In MF, the stainless-steel outer layer's stainless-steel outer layer CFD analysis and adjustment were limited by the bottom heat flux.

2.2.3 Electromagnetic field analysis

The equations of Maxwell serve as the foundation for the electromagnetic model. They are the Maxwell-Gauss equation, the Maxwell-Faraday equation, the Maxwell-Ampere equation, and the magnetic flux equation [22]:

$$\vec{\nabla} \cdot \vec{B} = 0 \quad (6)$$

$$\vec{\nabla} \cdot \vec{E} = 0 \quad (7)$$

$$\vec{\nabla} \times \vec{E} = -\frac{\partial \vec{B}}{\partial t} \quad (8)$$

$$\vec{\nabla} \times \vec{H} = \vec{J} + \frac{\partial \vec{D}}{\partial t} \quad (9)$$

where, \vec{B} denotes magnetic induction, \vec{E} denotes an electric field, \vec{H} denotes a magnetic field, \vec{J} denotes the electric current density related to free charges, and \vec{D} denotes the electric flux density. Additionally, we have the formulas shown below, which are for material properties [22]:

$$\vec{D} = \varepsilon \vec{E} \quad (10)$$

$$\vec{B} = \mu_m(T, \vec{H}) \vec{H} \quad (11)$$

$$\vec{J} = \sigma(\vec{T}) \vec{E} \quad (12)$$

where, σ an electrical conductivity dielectric constant is and magnetic permeability dielectric constants are ε , μ_m . In the case of low or medium frequencies.

$$\vec{B} = \vec{\nabla} \times \vec{A} \quad (13)$$

By using the following formula to the Maxwell-Ampere and Maxwell-Faraday equations, we can recast an electric field:

$$\vec{E} = -\frac{\partial \vec{A}}{\partial t} - \vec{\nabla} V \quad (14)$$

where, V stands for an electric scalar potential. Finally, we reach the equation shown below:

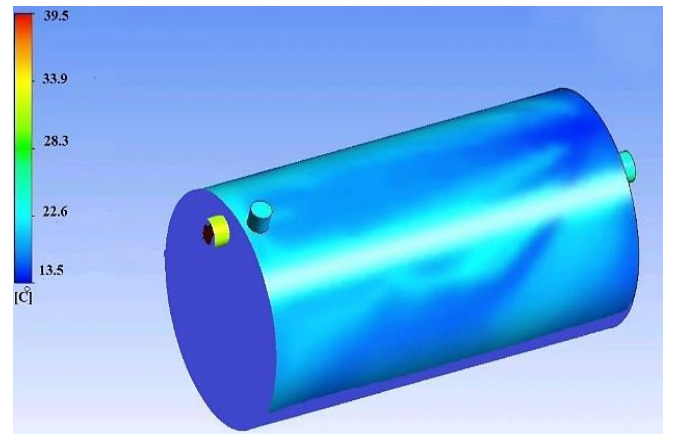
$$\sigma \frac{\partial \vec{A}}{\partial t} + \vec{\nabla} \times \left(\frac{1}{\mu_m} \vec{\nabla} \times \vec{A} \right) = -\sigma \vec{\nabla} V \quad (15)$$

when, σ is the conductance and (μ_m) is the magneto permeability. (σ) and (μ_m) both rely on temperatures and depends also in, \vec{H} the magnetic field. In actuality, the input current to be denoted by the right-hand phrase. We must add another equation in order to guarantee the solution's uniqueness. The Coulomb gauge describes the most frequent circumstance as follows [22]:

$$\vec{\nabla} \cdot \vec{A} = 0 \quad (16)$$

3. RESULTS AND DISCUSSION

We utilized the finite volume method-based program STORM/CFD2000 (Simunet Corp., CA, USA) to simulate the convective water flow in the heater through IH and MF. Calculations for the lower and top halves of the heater were produced in order to speed up the computing process. It is vital to measure the heat flow when a heating condition changes since the heat flow varies depending on the heating circumstances. On the other hand, when we can estimate heat formation in IH using electromagnetic the field analysis, we do not need to observe the heat flux (EFA). The water carrier is then heated in IH by dispersing heat along a 200 mm long, 16 mm diameter coil. The vortex heat is dispersed in a vessel with a diameter at 120 mm and a length at 250 mm. We have assumed that in the MF heat distribution, there is a thin layer of heat generation of 0.08 mm in the stainless-steel bottom plate, at the base of the vessel with a diameter of 100 mm, in a DC rotating motor, it produces magnetic vortices to produce heat at heater base. The distribution of heat generated at the heater's base is depicted in Figure 4. The distribution is depicted in this picture both horizontally and vertically. The top of the heater's temperature distribution is likewise seen in Figure 5. CFD was used to model the temperature distribution based on the thermogenesis distribution.



(A) Top section

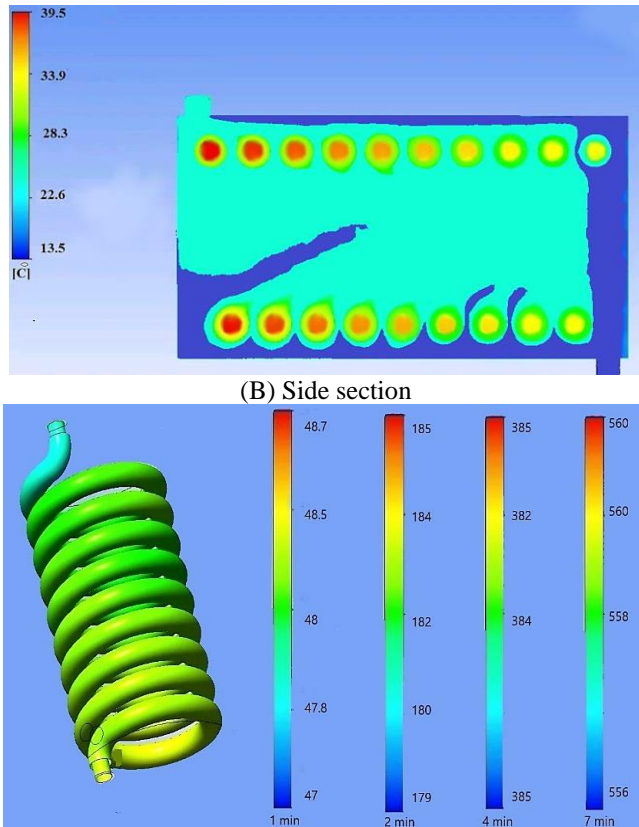


Figure 4. Temperature distribution generated by IH (A, B)

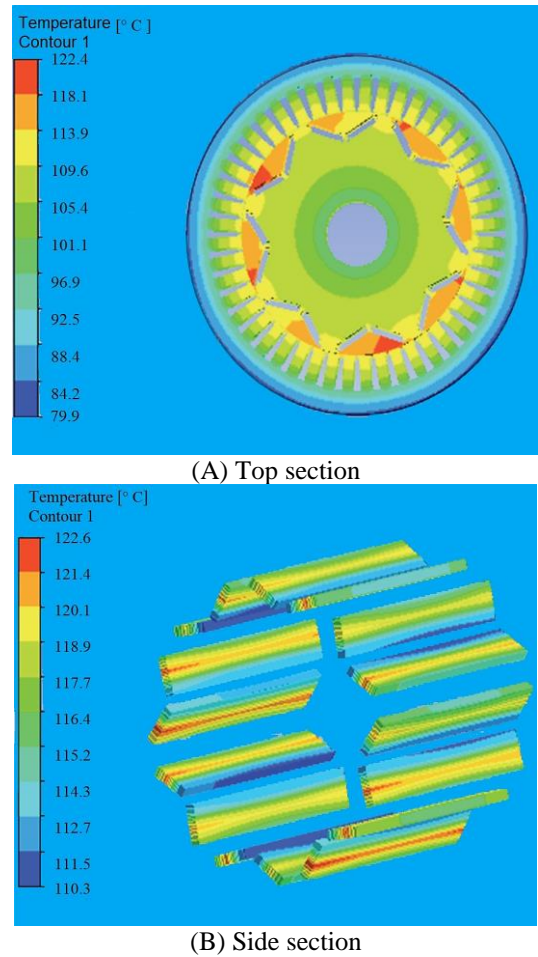


Figure 6. Temperature distribution generated by MF (A, B)

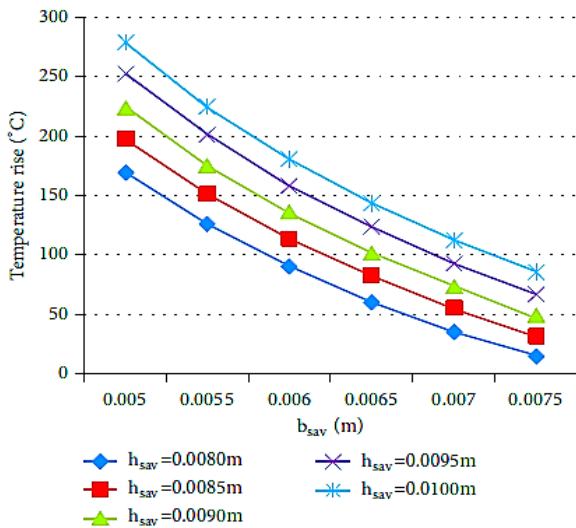


Figure 5. The rate of temperature rises by changing the size of the plates (b_{sav} , h_{sav})

Figure 6A (top view) and Figure 6B show the temperature distribution in heat radiation after the heater blank has been heated by MF for 30 seconds (side view). The temperature distribution for IH is depicted similarly in Figures 5A (top view) and 5B (side view). In MF, a doughnut-shaped heating pattern was used to raise the temperature of the heated area at the bottom of the heater, which is located just above the static magnet. The area around the heater's bottom corner in MF was warmer than the surrounding air. Due to the coil covering the majority of the heater's sides, the side heater has a high temperature. Therefore, the only portion of the bottom was heated on IH, whereas a large area, including a heater's bottom side, was heated in MF.

An appropriate electrode match is chosen in accordance with the MF design specifications. The length of the rotor core and its outer diameter are measured. The computed flux density takes the stated rotational speed into account. Calculations for the stator inner diameter and tooth width are made using (8) and (10). The stator hole's form is chosen after careful adjustment. The rise in temperature of the motor windings is assessed and calculated. The motor inner diameter D_{is} , tooth width b_{ts} , and slit height h_s should be modified until the temperature increase criteria are satisfied. In order to determine the electromagnetic density, we used the baseline values of 100 mm for the outer diameter, 48 holes and 8 poles for the shaft aperture, and 2000 rpm for the rated rotating speed. One can initially estimate the stator D_{is} inner diameter from (8). K_{Fes} and B_δ have fundamental stacking moduli of 0.97 and 0.6T, respectively. In Figure 5, the stator slot temperature rise curves are shown against the equivalent stator slot height and width. It is clear that the stator slot temperature rise is inversely proportional to the equivalent b_{sav} slot width and proportional to the equivalent h_{sav} stator equivalent height. We create a rotating structure, estimate the motor's maximum temperature rise, take into account the ambient temperature of 35°C, and then design the prototype device's primary features and specifications. According to control circuit coupling simulation, the average electromagnetism torque in Figure 7 is 210.7 N m, taking into account the circuit's multi-physics field, which includes electromagnetism, fluids, and temperature. We used the low voltage DC power supply of 12-48V, the maximum current at 20A, and the maximum power at 1000 W to determine the temperature distributions for the main motor

components of the vehicle's permanent magnet motor in operation at a speed of 2000 r/min while taking harmonic loss of the inverter into consideration (Figure 6). Rotor core and permanent magnet peak temperatures were 122.2°C and 122.6°C, respectively.

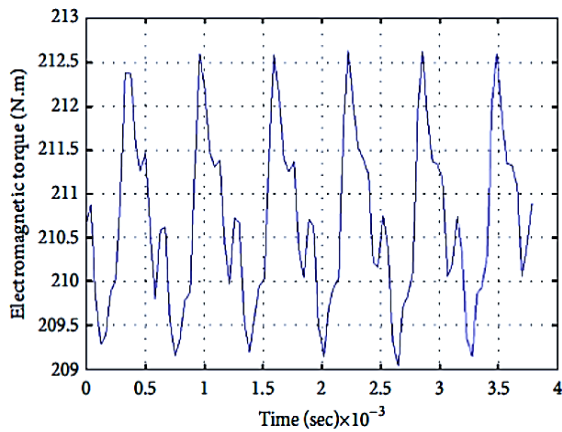


Figure 7. Electromagnetic torque simulation wavelength

Calculations of the evaporation rate in the case of magnetic field and induction compared with the theoretical results obtained from the equations, we can see from Figure 8.

Where we can see the relationship between evaporation rate and time, an increase on evaporation time led to an increase on the evaporation rate, a slight increase in evaporation rates occurred for the use of induction compared to magnetic field.

Figures 9A and B show the results for a flow velocity at around 7 minutes on heating in IH and MF, respectively, as a worst-case scenario at highest temperature used during heating in this experiment. By using CFD, it was possible to determine the typical flow velocity at the locations where the tracer particles are always found. A lower heating temperature was presumed, as seen in Figure 9 (a) and (b). Although it is thought that no water vapor is transferred, some heat may dissipate from the surface. The estimated value of flow velocity at IH and the actual measured value agree well. Because some of the calculated flow velocity numbers in MF were lower than the actual measured values, certain mistakes from model simplification may have occurred.

It should be noted that if the location-dependent convection in a vessel is taken into consideration, the CFD analysis might perform a detailed estimation of the convective flow of the heated water in IH, MF. It is important to look into the two phases of boiling water under IH and MF.

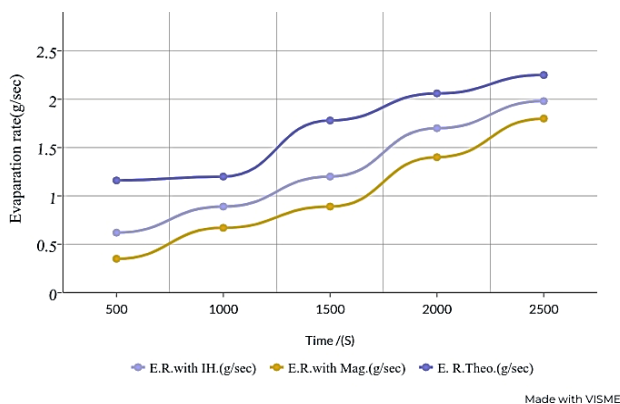
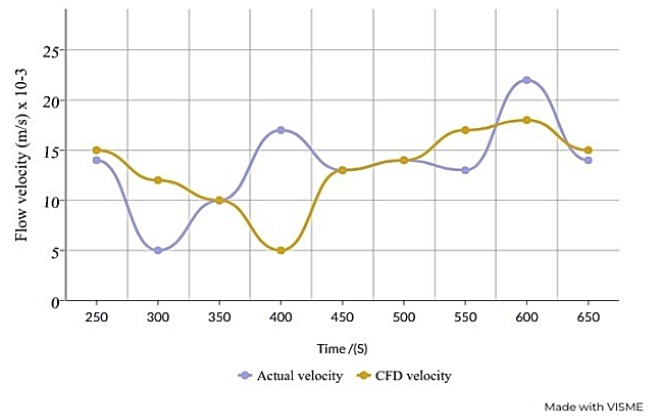
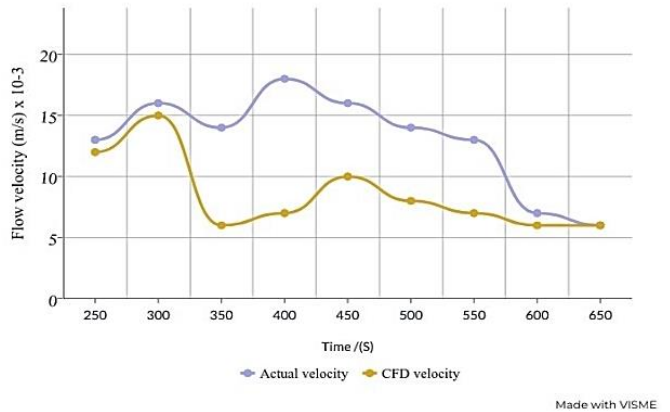


Figure 8. Water evaporation rate against time for induction and magnetic field



(a) IH



(b) MF

Figure 9. Compare measured and calculated a flow velocity: (a) under IH; (b) under MF

4. CONCLUSIONS

A CFD was used to examine convection in an IH- and MF-heated water heater. In IH, the upper portion of the heater was equipped with the heat generating distribution discovered through electromagnetic analysis. The bottom of the heater in the MF was placed to receive the heat flux distribution that was determined by the analysis of the magnetic field. The CFD-calculated rate of rise in water temperature is compatible with the outcome of the theoretical calculation. Particularly during the beginning stages of heating, the direction of convection and its resulting velocity varied between heating devices. However, at higher heating temperatures, the resulting velocity is similar for both methods of heating. Therefore, a CFD analysis can reasonably estimate the speed and direction of the convective flow in the heater. Calculations were made for the lower and upper halves of the heater in order to speed up the computing process. It is very important to measure heat flux when the heating state changes since heat flux vary with different heating conditions. On the other hand, when we can estimate heat formation in IH using electromagnetic field analysis, we do not need to observe heat flux (EFA). The IH water carrier is then heated by dispersing the heat along a 200 mm, 16 mm diameter coil. The vortex heat is dispersed in a vessel with a diameter of 120 mm and a length of 250 mm. We hypothesized that in the MF heat distribution, a 0.08 mm thin layer of heat generation in a stainless steel bottom plate, at the base of a 100 mm diameter vessel, in a DC rotary motor, produces magnetic vortices to produce heat at the base of the heater. The distribution of the

heat generated at the base of the heater reaches 120°C. The temperature distribution of IH similarly reaches 40°C. In the MF, a donut-shaped heating pattern was used to raise the temperature of the heated area at the bottom of the heater, which sits directly above the stationary magnet. The area around the bottom corner of the heater in the MF was warmer than the surrounding air. Since the coil covers the majority of the sides of the heater, the side heater has a high temperature. Therefore, only the underside was heated on IH, while a large area, including the underside of the heater, was heated on MF.

ACKNOWLEDGMENT

Authors acknowledge the support of Al-Mustaqbal University College in completing this work.

REFERENCES

- [1] Pang, X.F., Deng, B. (2008). The changes of macroscopic features and microscopic structures of water under influence of magnetic field. *Physica B: Condensed Matter*, 403(19-20): 3571-3577. <https://doi.org/10.1016/j.physb.2008.05.032>
- [2] Han, X., Peng, Y., Ma, Z. (2016). Effect of magnetic field on optical features of water and KCl solutions. *Optik*, 127(16): 6371-6376. <https://doi.org/10.1016/j.ijleo.2016.04.096>
- [3] Holysz, L., Szczes, A., Chibowski, E. (2007). Effects of a static magnetic field on water and electrolyte solutions. *Journal of Colloid and Interface Science*, 316(2): 996-1002. <https://doi.org/10.1016/j.jcis.2007.08.026>
- [4] Amiri, M.C., Dadkhah, A.A. (2006). On reduction in the surface tension of water due to magnetic treatment. *Colloids and Surfaces A: Physicochemical and Engineering Aspects*, 278(1-3): 252-255. <https://doi.org/10.1016/j.colsurfa.2005.12.046>
- [5] Wang, Y., Zhang, B., Gong, Z., Gao, K., Ou, Y., Zhang, J. (2013). The effect of a static magnetic field on the hydrogen bonding in water using frictional experiments. *Journal of Molecular Structure*, 1052: 102-104. <https://doi.org/10.1016/j.molstruc.2013.08.021>
- [6] Cai, R., Yang, H., He, J., Zhu, W. (2009). The effects of magnetic fields on water molecular hydrogen bonds. *Journal of Molecular Structure*, 938(1-3): 15-19. <https://doi.org/10.1016/j.molstruc.2009.08.037>
- [7] Toledo, E.J., Ramalho, T.C., Magriotis, Z.M. (2008). Influence of magnetic field on physical–Chemical properties of the liquid water: Insights from experimental and theoretical models. *Journal of Molecular Structure*, 888(1-3): 409-415. <https://doi.org/10.1016/j.molstruc.2008.01.010>
- [8] Chang, K.T., Weng, C.I. (2006). The effect of an external magnetic field on the structure of liquid water using molecular dynamics simulation. *Journal of Applied Physics*, 100(4): 043917. <https://doi.org/10.1063/1.2335971>
- [9] Liu, B., Gao, B., Xu, X., Hong, W., Yue, Q., Wang, Y., Su, Y. (2011). The combined use of magnetic field and iron-based complex in advanced treatment of pulp and paper wastewater. *Chemical Engineering Journal*, 178: 232-238. <https://doi.org/10.1016/j.cej.2011.10.058>
- [10] Kobe, S., Dražić, G., McGuinness, P.J., Stražisar, J. (2001). The influence of the magnetic field on the crystallisation form of calcium carbonate and the testing of a magnetic water-treatment device. *Journal of Magnetism and Magnetic Materials*, 236(1-2): 71-76. [https://doi.org/10.1016/S0304-8853\(01\)00432-2](https://doi.org/10.1016/S0304-8853(01)00432-2)
- [11] Maffei, M.E. (2014). Magnetic field effects on plant growth, development, and evolution. *Frontiers in Plant Science*, 5: 445. <https://doi.org/10.3389/fpls.2014.00445>
- [12] Castillo, J.P., Martínez, J., Riofrio, A.J., Villacis, S.P., Orozco, M.A. (2015). Computational fluid dynamic analysis of olive oil in different induction pots. In 1st Pan-American Congress on Computational Mechanics–PANACM, Argentina, pp. 729-741.
- [13] FRPERC. (1995). CFD in the food industry. *Food Refrigeration and Process Engineering Research Centre Newsletter*, 10: 1-2.
- [14] Xia, B., Sun, D.W. (2002). Applications of computational fluid dynamics (CFD) in the food industry: A review. *Computers and Electronics in Agriculture*, 34(1-3): 5-24. [https://doi.org/10.1016/S0168-1699\(01\)00177-6](https://doi.org/10.1016/S0168-1699(01)00177-6)
- [15] Norton, T., Sun, D.W. (2006). Computational fluid dynamics (CFD)–An effective and efficient design and analysis tool for the food industry: A review. *Trends in Food Science & Technology*, 17(11): 600-620. <https://doi.org/10.1016/j.tifs.2006.05.004>
- [16] Gandhi, M.S., Sathe, M.J., Joshi, J.B., Vijayan, P.K. (2011). Two phase natural convection: CFD simulations and PIV measurement. *Chemical Engineering Science*, 66(14): 3152-3171. <https://doi.org/10.1016/j.ces.2011.02.060>
- [17] Kumar, V., Wee, A.P., Birla, S., Subbiah, J., Thippareddi, H. (2012). A 3-D computational fluid dynamics model for forced air cooling of eggs placed in trays. *Journal of Food Engineering*, 108(3): 480-492. <https://doi.org/10.1016/j.jfoodeng.2011.08.003>
- [18] Ghani, A.A., Farid, M.M., Zarrouk, S.J. (2003). The effect of can rotation on sterilization of liquid food using computational fluid dynamics. *Journal of Food Engineering*, 57(1): 9-16. [https://doi.org/10.1016/S0260-8774\(02\)00215-7](https://doi.org/10.1016/S0260-8774(02)00215-7)
- [19] Naar, R., Bay, F. (2013). Numerical optimisation for induction heat treatment processes. *Applied Mathematical Modelling*, 37(4): 2074-2085. <https://doi.org/10.1016/j.apm.2012.04.058>
- [20] Shokouhmand, H., Ghaffari, S. (2012). Thermal analysis of moving induction heating of a hollow cylinder with subsequent spray cooling: Effect of velocity, initial position of coil, and geometry. *Applied Mathematical Modelling*, 36(9): 4304-4323. <https://doi.org/10.1016/j.apm.2011.11.058>
- [21] Jassim, L., Elmnifi, M., Elbreki, A., Habeeb, L.J. (2022). Modeling and analysis of home heating system material performance with induction using solar energy. *Materials Today: Proceedings*, 61: 852-859. <https://doi.org/10.1016/j.matpr.2021.09.302>
- [22] Majdi, H.S., Habeeb, L.J., Elmnifi, M., Alderoubi, N. (2022). Transient free convection between two horizontal concentric cylinders. *International Journal of Mechanical Engineering*, 7(1): 596-609. <https://doi.org/10.56452/2022-7-0022>
- [23] Ebrahim, S.A., Azab, A.E. (2017). Biological effects of magnetic water on human and animals. *Biomedical Sciences*, 3(4): 78-85.

- <https://doi.org/10.11648/j.bs.20170304.12>
- [24] Sronsri, C., Kongpop, U., Sittipol, W. (2020). Quantitative analysis of calcium carbonate formation in magnetized water. *Materials Chemistry and Physics*, 245: 122735. <https://doi.org/10.1016/j.matchemphys.2020.122735>
- [25] El-Sabrou, K., El-Hanoun, A. (2019). Does magnetised drinking water influence poultry's health and production? *World's Poultry Science Journal*, 75(3): 411-416. <https://doi.org/10.1017/S0043933919000266>
- [26] Elmnifi, M., Moria, H., Elbreki, A.M., Abdulrazig, O.D. (2021). Possibilities study of using hybrid solar collectors in northeastern Libya residential home. *International Journal of Renewable Energy Research (IJRER)*, 11(2): 654-661.
- [27] Jenkins, P., Elmnifi, M., Younis, A., Emhamed, A. (2019). Hybrid power generation by using solar and wind energy: Case study. *World Journal of Mechanics*, 9(4): 81-93. <https://doi.org/10.4236/wjm.2019.94006>
- [28] Boadi, A., Tsuchida, Y., Todaka, T., Enokizono, M. (2005). Designing of suitable construction of high-frequency induction heating coil by using finite-element method. *IEEE Transactions on Magnetics*, 41(10): 4048-4050. <https://doi.org/10.1109/TMAG.2005.854993>
- [29] Fu, X., Wang, B., Tang, X., Ji, H., Zhu, X. (2017). Study on induction heating of workpiece before gear rolling process with different coil structures. *Applied Thermal Engineering*, 114: 1-9. <https://doi.org/10.1016/j.applthermaleng.2016.11.192>

NOMENCLATURE

A	Area (m^2)
C_p	Specific heat ($J/kg \cdot ^\circ C$)
G	Acceleration due to gravity (m/s^2)
H	Heat transfer coefficient ($W/m^2 \cdot ^\circ C$)
K	Thermal conductivity ($W/m \cdot ^\circ C$)
P	Static pressure (N/m^2)
Q	Heat flow (W/m^2)
t	Time (s)
T	Temperature ($^\circ C$)
v	Speed (m/s)
V	Electric potential
\vec{A}	Magnetic bus voltage (V s/m)
\vec{B}	Magnetic induction (N s/C m)
\vec{D}	Electric flux density (C/m^2)
\vec{E}	Electric field (V/m)
H	Magnetic field (Am)
J	Electric current density (A/m^2)
β	Thermal expansion coefficient ($1/K$)
ϵ	Dielectric constant (F/m)
δ	Electrical conductivity (S/m)
ρ	Density (kg/m^3)
μ	Apparent viscosity (Pa)
μ_m	Magnetic permeability lm (N/A^2) texts
R, θ, z	Radial, angle, and perpendicular direction of the pan
Ref	References
w	Wall